



Relaxation-Diffusion Spectrum Imaging for Probing Tissue Microarchitecture

Ye Wu^{1(✉)}, Xiaoming Liu², Xinyuan Zhang³, Khoi Minh Huynh^{4,5}, Sahar Ahmad^{4,5},
and Pew-Thian Yap^{4,5(✉)}

¹ School of Computer Science and Engineering, Nanjing University of Science and Technology, Nanjing, China
wuye@njjust.edu.cn

² Union Hospital, Tongji Medical College, Huazhong University of Science and Technology, Wuhan, Hubei, China

³ School of Biomedical Engineering, Southern Medical University, Guangzhou, China

⁴ Department of Radiology, University of North Carolina, Chapel Hill, NC, USA

⁵ Biomedical Research Imaging Center, University of North Carolina, Chapel Hill, NC, USA
ptyap@med.unc.edu

Abstract. Brain tissue microarchitecture is characterized by heterogeneous degrees of diffusivity and rates of transverse relaxation. Unlike standard diffusion MRI with a single echo time (TE), which provides information primarily on diffusivity, relaxation-diffusion MRI involves multiple TEs and multiple diffusion-weighting strengths for probing tissue-specific coupling between relaxation and diffusivity. Here, we introduce a relaxation-diffusion model that characterizes tissue apparent relaxation coefficients for a spectrum of diffusion length scales and at the same time factors out the effects of intra-voxel orientation heterogeneity. We examined the model with an *in vivo* dataset, acquired using a clinical scanner, involving different health conditions. Experimental results indicate that our model caters to heterogeneous tissue microstructure and can distinguish fiber bundles with similar diffusivities but different relaxation rates. Code with sample data is available at <https://github.com/dryewu/RDSI>.

Keywords: Diffusion MRI · Microstructure · Relaxation diffusion

1 Introduction

Recent advances in diffusion MRI (dMRI) and diffusion signal modeling equip brain researchers with an *in vivo* probe into microscopic tissue compositions [15, 21]. Signal differences between water molecules in restricted, hindered, and free compartments

Y. Wu and X. Liu—Contributed equally to the paper.

This work was supported by the National Natural Science Foundation of China (No. 62201265, 61971214), and the Natural Science Foundation of Hubei Province of China (No. 2021CFB442). P.-T. Yap was supported in part by the United States National Institutes of Health (NIH) through grants MH125479 and EB008374.

can be characterized by higher-order diffusion models for estimating the relative proportions of cell bodies, axonal fibers, and interstitial fluids within an imaging voxel. This allows for the detection of tissue compositional changes driven by development, degeneration, and disorders [13, 22]. However, accurate characterization of tissue composition is not only affected by compartment-specific diffusivities but also transverse relaxation rates [4, 27]. Several studies have shown that explicit consideration of the relaxation-diffusion coupling may improve the characterization of tissue microstructure [6, 16, 25].

Multi-compartment models are typically used to characterize signals from, for example, intra- and extra-neurite compartments [18, 29]. However, due to the multitude of possible compartments and fiber configurations, solving for these models can be challenging. The problem can be simplified by considering per-axon diffusion models [8, 10, 28], which typically factor out orientation information and hence involve less parameters. However, existing models are typically constrained to data acquired with a single TE (STE) and do not account for compartment-specific T_2 relaxation. Several studies have shown that multi-TE (MTE) data can account better for intravoxel architectures and fiber orientation distribution functions (fODFs) [1, 6, 16, 17, 19].

Here, we propose a unified strategy to estimate using MTE diffusion data (i) compartment specific T_2 relaxation times; (ii) non- T_2 -weighted (non- T_2w) parameters of multi-scale microstructure; and (iii) non- T_2w multi-scale fODFs. Our method, called relaxation-diffusion spectrum imaging (RDSI), allows for the direct estimation of non- T_2w volume fractions and T_2 relaxation times of tissue compartments. We evaluate RDSI using both ex vivo monkey and in vivo human brain MTE data, acquired with fixed diffusion times across multiple b-values. Using RDSI, we demonstrate the TE dependence of T_2w fODFs. Furthermore, we show the diagnostic potential of RDSI in differentiating tumors and normal tissues.

2 Methods

2.1 Multi-compartment Model

The diffusion-attenuated signal $S(\tau, b, \mathbf{g})$ acquired with TE τ , diffusion gradient vector \mathbf{g} , and gradient strength b can be modeled as

$$S(\tau, b, \mathbf{g}) \approx S(b, \mathbf{g})e^{-\frac{\tau}{T_2(b)}}, \quad (1)$$

which can be expanded to a multi-compartment model:

$$S(\tau, b, \mathbf{g}) \approx S_r(b, \mathbf{g})e^{-\tau r_r(b)} + S_h(b, \mathbf{g})e^{-\tau r_h(b)} + S_f(b)e^{-\tau r_f(b)} \quad (2)$$

to account for signals $S_r(b, \mathbf{g})$, $S_h(b, \mathbf{g})$, and $S_f(b)$ and T_2 values of restricted, hindered, and free compartments. The apparent relaxation rates at different b-values, $r(b) = 1/T_2(b)$, can be estimated using single-shell data acquired with two or more TEs [14]. This model can be expressed using spherical deconvolution [9]:

$$\begin{aligned}
S(\tau, b, \mathbf{g}) = & e^{-\tau r_r(b)} \int_{D_r} R(b, \mathbf{g}, D_r) f(D_r) dD_r + e^{-\tau r_h(b)} \int_{D_h} R(b, \mathbf{g}, D_h) f(D_h) dD_h \\
& + e^{-\tau r_f(b)} \int_{D_f} R(b, D_f) f(D_f) dD_f \\
\text{s.t. } & r_r(b), r_h(b), r_f(b) \geq 0 \forall b, \mathcal{A}f(D_r), \mathcal{A}f(D_h), \mathcal{A}f(D_f) \geq 0,
\end{aligned} \tag{3}$$

where the compartment-specific response functions $R(b, \mathbf{g}, D_r)$, $R(b, \mathbf{g}, D_h)$, and $R(b, D_f)$ are associated with apparent diffusion coefficients D_r , D_h , and D_f , yielding compartment-specific multi-scale fODFs $f(D_r)$, $f(D_h)$, and $f(D_f)$. Operator \mathcal{A} relates the spherical harmonics coefficients to fODF amplitudes.

2.2 Model Simplification via Spherical Mean

The spherical mean technique (SMT) [10] focuses on the direction-averaged signal to factor out the effects of the fiber orientation distribution. Taking the spherical mean, (3) can be written as

$$\begin{aligned}
\bar{S}(\tau, b) = & e^{-\tau r_r(b)} \int_{D_r} k(b, D_r) w(D_r) dD_r + e^{-\tau r_h(b)} \int_{D_h} k(b, D_h) w(D_h) dD_h \\
& + e^{-\tau r_f(b)} \int_{D_f} k(b, D_f) w(D_f) dD_f \\
\text{s.t. } & r_r(b), r_h(b), r_f(b) \geq 0 \forall b, w(D_r), w(D_h), w(D_f) \geq 0
\end{aligned} \tag{4}$$

where $w(D_r)$, $w(D_h)$, and $w(D_f)$ are volume fractions and $k(b, D_r)$, $k(b, D_h)$, and $k(b, D_f)$ are spherical means of response functions $R(b, \mathbf{g}, D_r)$, $R(b, \mathbf{g}, D_h)$, and $R(b, D_f)$, respectively. Based on [8, 10], spherical means can be written as:

$$\begin{aligned}
k(b, D_r) \equiv k(b, \{\lambda_{\parallel}, \lambda_{\perp}\} \in \Lambda_r) &= e^{-b\lambda_{\perp}} \frac{\sqrt{\pi} \operatorname{erf}(\sqrt{b(\lambda_{\parallel} - \lambda_{\perp})})}{2\sqrt{b(\lambda_{\parallel} - \lambda_{\perp})}}, \quad \frac{\lambda_{\parallel}}{\lambda_{\perp}} \asymp \phi^2, \\
k(b, D_h) \equiv k(b, \{\lambda_{\parallel}, \lambda_{\perp}\} \in \Lambda_h) &= e^{-b\lambda_{\perp}} \frac{\sqrt{\pi} \operatorname{erf}(\sqrt{b(\lambda_{\parallel} - \lambda_{\perp})})}{2\sqrt{b(\lambda_{\parallel} - \lambda_{\perp})}}, \quad 1 \prec \frac{\lambda_{\parallel}}{\lambda_{\perp}} \prec \phi^2, \\
k(b, D_f) \equiv k(b, \{\lambda_{\parallel}, \lambda_{\perp}\} \in \Lambda_f) &= e^{-b\lambda_{\perp}}, \quad \lambda_{\parallel} = \lambda_{\perp},
\end{aligned} \tag{5}$$

where D_r , D_h , and D_f are parameterized by parallel diffusivity λ_{\parallel} and perpendicular diffusivity λ_{\perp} for the restricted (Λ_r), hindered (Λ_h) and free (Λ_f) compartments. ϕ is the geometric tortuosity [28]. The spherical mean signal can thus be seen as the weighted combination of the spherical mean signals of spin packets. Similar to [8, 28], (4) allows us to probe the relaxation-diffusion coupling across a spectrum of diffusion scales. Anisotropic diffusion can be further separated as restricted or hindered.

2.3 Estimation of Relaxation and Diffusion Parameters

We first solve for the relaxation modulated spherical mean coefficients in (4). Next, we disentangle the relaxation terms from the spherical mean coefficients and solve for the relaxation rates. Finally, we estimate the fODFs using (3). Details are provided below:

(i) *Relaxation modulated spherical mean coefficients.* We rewrite (4) in matrix form as

$$\bar{\mathbf{S}} = \mathbf{K}\mathbf{E} \circ \mathbf{W} = \mathbf{K}\mathbf{X}, \quad (6)$$

where the mean signal $\bar{\mathbf{S}}$ is expressed as the product of the response function spherical mean matrix \mathbf{K} and the Kronecker product (\circ) of relaxation matrix \mathbf{E} and volume fraction matrix \mathbf{W} . We can solve for \mathbf{X} in (6) via an augmented problem with the OSQP solver¹:

$$\arg \min_{\mathbf{X} \succeq 0} \frac{1}{2} \|\mathbf{K}\mathbf{X} - \bar{\mathbf{S}}\|_2^2. \quad (7)$$

(ii) *Relaxation times.* With \mathbf{X} solved, \mathbf{E} and \mathbf{W} can be determined by minimizing a constrained non-linear multivariate problem:

$$\min_{\mathbf{E}, \mathbf{W}} \frac{1}{2} \|\mathbf{E} \circ \mathbf{W} - \bar{\mathbf{X}}\|_2^2 \text{ s.t. } \mathbf{E} \geq 0, \mathbf{W} \geq 0, \sum \mathbf{W} = 1, \quad (8)$$

which can be solved using a gradient based optimizer. Relaxation times can be determined based on \mathbf{E} .

(iii) *fODFs.* With \mathbf{E} determined, (3) can be rewritten as a strictly convex quadratic programming (QP) problem:

$$\hat{\mathbf{f}} = \arg \min_{\mathbf{f}} \frac{1}{2} \mathbf{f}^\top \mathbf{P} \mathbf{f} + \mathbf{Q}^\top \mathbf{f}, \text{ s.t. } \mathbf{A}\mathbf{f}(D_r), \mathbf{A}\mathbf{f}(D_h), \mathbf{A}\mathbf{f}(D_f) \geq 0, \forall D_r, \forall D_h, \forall D_f, \quad (9)$$

which can be solved using the OSQP solver.

2.4 Microstructure Indices

Based on (3) and (4), various microstructure indices can be derived:

- Microscopic fractional anisotropy [20], per-axon axial and radial diffusivity [2], and free and restricted isotropic diffusivity.
- Axonal morphology indices derived based on [17, 26] to compute the mean neurite radius (Mean NR), its internal deviation (Std. NR), and relative neurite radius (Cov. NR):
 - Mean NR = $\text{mean}(\epsilon(\delta, \Delta) w_{D_r} \lambda_{\parallel} \lambda_{\perp})^{1/4}$, $\{\lambda_{\parallel}, \lambda_{\perp}\} \in D_r$, where $\epsilon \succ 0$ is a pulse scale that only depends on the pulse width δ and diffusion time Δ of the diffusion gradients.
 - Std. NR = $\text{std}((\epsilon(\delta, \Delta) w_{D_r} \lambda_{\parallel} \lambda_{\perp})^{1/4})$.
 - Cov. NR = $\text{cov}((\epsilon(\delta, \Delta) w_{D_r} \lambda_{\parallel} \lambda_{\perp})^{1/4}) \equiv \text{cov}((w_{D_r} \lambda_{\parallel} \lambda_{\perp})^{1/4})$, which is independent on ϵ .

¹ <https://osqp.org/>.

2.5 Data Acquisition and Processing

Ex Vivo Data. We used an ex vivo monkey dMRI dataset² collected with a 7T MRI scanner [19]. A single-line readout PGSE sequence with pulse duration $\delta = 9.6$ ms and separation $\Delta = 17.5$ ms, echo times $TE = \{35.5, 45.5\}$ ms, $TR = 3500$ ms, and 0.5 mm isotropic resolution was utilized for acquisition across five shells, $b = \{4, 7, 23, 27, 31\} \times 10^3$ s/mm², each with a common set of 96 non-collinear gradient directions. A $b = 0$ s/mm² image was also acquired.

In Vivo Data. One healthy subject and three patients with gliomas were scanned using a Philips Ingenia CX 3T MRI scanner with a gradient strength of 80 mT/m and switching rates of 200 mT/m/ms. Diffusion data with seven TEs were obtained using a spin-echo echo-planar imaging sequence with fixed TR and diffusion time, $\{4, 4, 8, 8, 16\}$ diffusion-encoding directions at $b = \{0, 4, 8, 16, 32\} \times 10^2$ s/mm² respectively, $TE = \{75, 85, 95, 105, 115, 125, 135\}$ ms, $TR = 4000$ ms, 1.5 mm isotropic voxel size, image size = 160×160 , 96 slices, whole-brain coverage, and acceleration factor = 3. The total imaging time was 21 min. Data processing includes (i) noise level estimation and removal; (ii) Rician unbiasing; (iii) removal of Gibbs ringing artifacts; and (iv) motion and geometric distortion corrections. To compensate for motion, all dMRIs were first preprocessed separately and then aligned using rigid registration based on the non-diffusion-weighted images. The lowest TE was set to minimize the contribution of the myelin water to the measured signal and the largest TE was chosen as a trade-off between image contrast and noise. Following previous studies [6, 16] and in-house testing, we used a spectrum of TE scales from 75 to 135 ms to cover tissue heterogeneity. We used MRtrix³ to generate tissue segmentations (cortical and subcortical GM, WM, CSF, and pathological tissue) based on the T1w data.

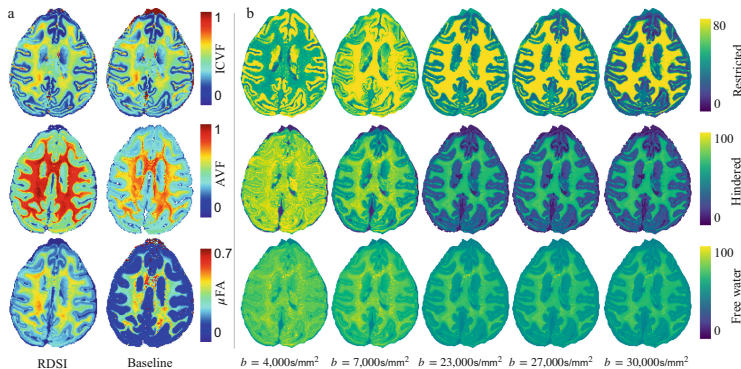


Fig. 1. Ex vivo data. (a) RDSI and REDIM parameter maps for tissue microstructure; (b) RDSI relaxation times for diffusion compartments.

² <https://resources.drcmr.dk/MAPdata/axon-relaxation/>.

³ <https://www.mrtrix.org/>.

Implementation. To cover the whole diffusion spectrum, we set the diffusivity from 0 s/mm^2 (no diffusion) to $3 \times 10^{-3} \text{ s/mm}^2$ (free diffusion). For the anisotropic compartment, λ_{\parallel} was set from $1.5 \times 10^{-3} \text{ mm}^2/\text{s}$ to $2 \times 10^{-3} \text{ mm}^2/\text{s}$. Radial diffusivity λ_{\perp} was set to satisfy $\lambda_{\parallel}/\lambda_{\perp} \geq 1.1$ as in [8, 28]. For the isotropic compartment, we set the diffusivity $\lambda_{\parallel} = \lambda_{\perp}$ from $0 \text{ mm}^2/\text{s}$ to $3 \times 10^{-3} \text{ mm}^2/\text{s}$ with step size $0.1 \times 10^{-3} \text{ mm}^2/\text{s}$.

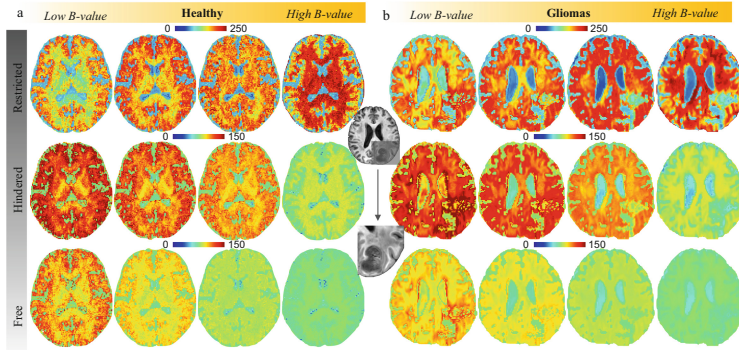


Fig. 2. In vivo data. Compartment-specific parameters for (a) healthy and (b) glioma subjects.

3 Results

3.1 Ex Vivo Data: Compartment-Specific Parameters

Figure 1(a) shows the estimated maps of T_2 -independent parameters given by a baseline comparison method, called REDIM [16], and RDSI. We observe that the two methods yield similar intracellular volume fraction (ICVF) estimates. However, REDIM overestimates the anisotropic volume fraction (AVF) compared to RDSI, resulting in blurred boundaries between the gray matter and superficial white matter. RDSI yields consistent distribution between ICVF and μFA maps.

Figure 1(b) shows the RDSI T_2 relaxation maps of restricted, hindered, and free diffusion across b-values. As the b-value increases, the relaxation time increases for the restricted component but decreases for the hindered and free components. At lower b-values, the relaxation time for the extra-neurite compartment is substantially higher than that of the intra-neurite compartment.

3.2 In Vivo Data: Compartment-Specific Parameters

Figure 2 shows the RDSI T_2 relaxation maps of restricted, hindered, and free diffusion across b-values. The values are consistent between healthy and glioma subjects. The estimated relaxation times are in general in line with previous reports [6, 11]. RDSI

shows substantial differences between tumor and normal tissues in the relaxation maps (Fig. 2(b)).

Figure 3 shows the voxel distributions with respect to relaxation times and b-values. It is apparent that at higher b-values, a greater fraction of voxels in the restricted compartment have relaxation times within 100 to 200 ms, particularly for higher-grade gliomas. This might be related to prolonged transverse relaxation time due to increased water content within the tumor [5, 7, 24]. This property is useful in the visualization of peritumoral edema, an area containing infiltrating tumor cells and increased extracellular water due to plasma fluid leakage from aberrant tumor capillaries that surrounds the tumor core in higher-grade gliomas.

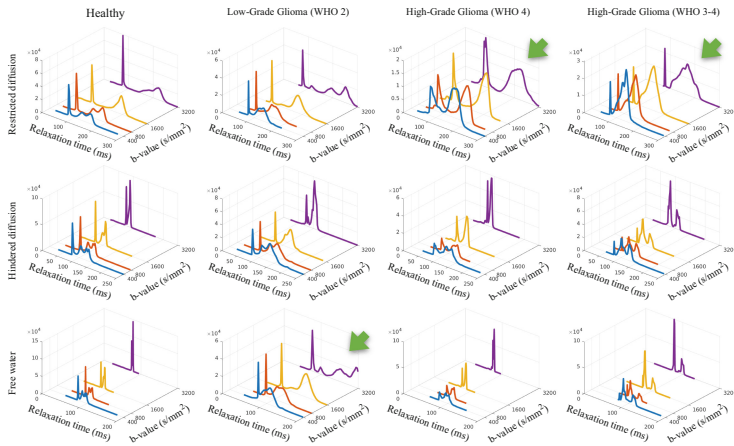


Fig. 3. Voxel distributions with respect to relaxation times and b-values.

3.3 In Vivo Data: Neurite Morphology

Figure 4(a) shows the relaxation times of the restricted compartment in white matter lesions, indicating that relaxation times are longer in gliomas than normal white matter tissue. The higher T_2 in grade 4 glioma is associated with changes in metabolite compositions, resulting in remarkable changes in neurite morphology in lesioned tissues (Fig. 4(c–d)), consistent with previous observations [12, 23]. The rate of longitudinal relaxation time has been shown to be positively correlated with myelin content. Our results indicate that MTE dMRI is more sensitive to neurite morphology than STE dMRI (Fig. 4(b)).

Figures 4(c–d) show that the estimated Mean NR in the gray matter is approximately in the range of $10 \mu\text{m}$, which is in good agreement with the sizes of somas in human brains, i.e., $11 \pm 7 \mu\text{m}$ [26]. RDSI improves the detection of small metastases, delineation of tumor extent, and characterization of the intratumoral microenvironment when compared to conventional microstructure models (Fig. 4(c)). Our studies suggest

that RDSI provides useful information on microvascularity and necrosis helpful for facilitating early stratification of patients with gliomas (Fig. 4(d)).

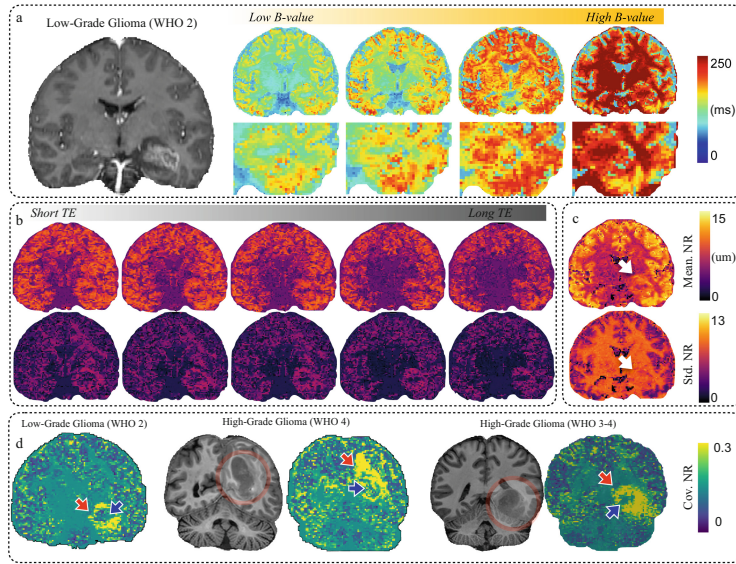


Fig. 4. Relaxation time of the restricted compartment of (a) a glioma patient, and (b) *TE*-dependent and (c-d) T_2 -independent neurite morphology.

3.4 Relation Between Relaxation and Diffusivity

Figure 5 shows the relaxation-diffusivity distributions of white matter (WM), cortical gray matter (GM), and subcortical gray matter (SGM). The 2D plots show the contours of the joint distributions of the relaxation and diffusivity values across all voxels. The average diffusivity and relaxation in these regions indicate the existence of a single homogeneous region in WM and SGM. For GM, however, we observe a small peak for the relaxation rate arange 1e-3 to 1.5e-3.

3.5 fODFs

Figure 6 shows that the reconstructed fODFs are consistent with the expected WM arrangement of the healthy human brain. We provide a visual comparison of the fODFs estimated with and without the explicit consideration of relaxation. The two cases yield different fODFs. As expected, fiber populations are associated with different relaxation times, in line with [3, 16]. Our studies suggest that this difference could be caused by the spatially heterogeneous tissue microstructure, since fiber bundles with slower relaxation times contribute less to diffusion signals acquired with a longer *TE*. Explicitly taking into account relaxation in our model results in noteworthy contrast improvement in spatially heterogeneous superficial WM.

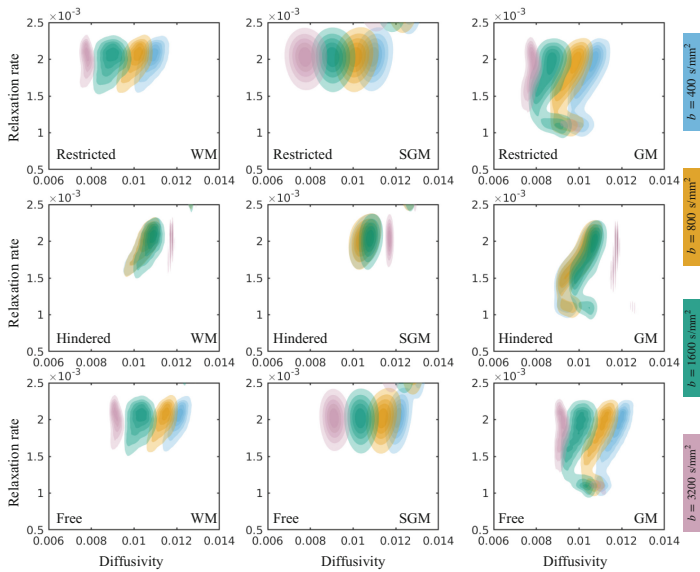


Fig. 5. Relaxation-diffusivity distributions for white matter (left), subcortical gray matter (middle), and cortical gray matter (right).

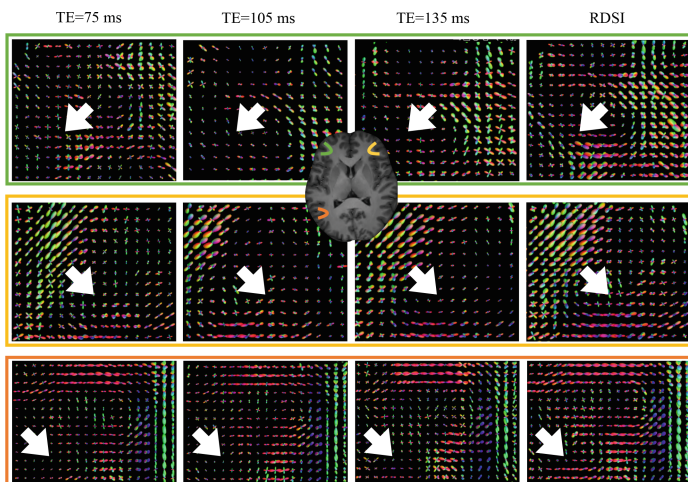


Fig. 6. TE-dependent and TE-independent fODFs in three superficial white matter regions.

4 Conclusion

RDSI provides a unified strategy for direct estimation of relaxation-independent volume fractions and compartment-specific relaxation times. Using MTE data, we demonstrated that RDSI can delineate heterogeneous tissue microstructure elusive to STE data. We also showed that RDSI provides information that is conducive to characterizing tissue abnormalities.

References

1. Anania, V., et al.: Improved diffusion parameter estimation by incorporating T2 relaxation properties into the DKI-FWE model. *Neuroimage* **256**, 119219 (2022)
2. Assaf, Y., Freidlin, R.Z., Rohde, G.K., Basser, P.J.: New modeling and experimental framework to characterize hindered and restricted water diffusion in brain white matter. *Magn. Reson. Med.* **52**(5), 965–978 (2004)
3. Barakovic, M., et al.: Bundle-specific axon diameter index as a new contrast to differentiate white matter tracts. *Front. Neurosci.* **15**, 646034 (2021)
4. Cowan, B., Cowan, B.P.: Nuclear Magnetic Resonance and Relaxation, vol. 427. Cambridge University Press, Cambridge (1997)
5. Ellingson, B.M., Wen, P.Y., Cloughesy, T.F.: Modified criteria for radiographic response assessment in glioblastoma clinical trials. *Neurotherapeutics* **14**(2), 307–320 (2017)
6. Gong, T., Tong, Q., He, H., Sun, Y., Zhong, J., Zhang, H.: MTE-NODDI: multi-TE NODDI for disentangling non-T2-weighted signal fractions from compartment-specific T2 relaxation times. *Neuroimage* **217**, 116906 (2020)
7. Hu, L.S., Hawkins-Daarud, A., Wang, L., Li, J., Swanson, K.R.: Imaging of intratumoral heterogeneity in high-grade glioma. *Cancer Lett.* **477**, 97–106 (2020)
8. Huynh, K.M., et al.: Probing tissue microarchitecture of the baby brain via spherical mean spectrum imaging. *IEEE Trans. Med. Imaging* **39**(11), 3607–3618 (2020)
9. Jeurissen, B., Tournier, J.D., Dhollander, T., Connelly, A., Sijbers, J.: Multi-tissue constrained spherical deconvolution for improved analysis of multi-shell diffusion MRI data. *Neuroimage* **103**, 411–426 (2014)
10. Kaden, E., Kelm, N.D., Carson, R.P., Does, M.D., Alexander, D.C.: Multi-compartment microscopic diffusion imaging. *Neuroimage* **139**, 346–359 (2016)
11. Lampinen, B., et al.: Towards unconstrained compartment modeling in white matter using diffusion-relaxation MRI with tensor-valued diffusion encoding. *Magn. Reson. Med.* **84**(3), 1605–1623 (2020)
12. Li, Y., Srinivasan, R., Ratiney, H., Lu, Y., Chang, S.M., Nelson, S.J.: Comparison of T1 and T2 metabolite relaxation times in glioma and normal brain at 3T. *J. Magn. Reson. Imaging* **28**(2), 342–350 (2008). <https://onlinelibrary.wiley.com/doi/10.1002/jmri.21453>
13. McDonald, E.S., et al.: Mean apparent diffusion coefficient is a sufficient conventional diffusion-weighted MRI metric to improve breast MRI diagnostic performance: results from the ECOG-ACRIN cancer research group A6702 diffusion imaging trial. *Radiology* **298**(1), 60 (2021)
14. McKinnon, E.T., Jensen, J.H.: Measuring intra-axonal T₂ in white matter with direction-averaged diffusion MRI. *Magn. Reson. Med.* **81**(5), 2985–2994 (2019)
15. Morozov, S., et al.: Diffusion processes modeling in magnetic resonance imaging. *Insights Imaging* **11**(1), 60 (2020)

16. Ning, L., Gagoski, B., Szczepankiewicz, F., Westin, C.F., Rathi, Y.: Joint relaxation-diffusion imaging moments to probe neurite microstructure. *IEEE Trans. Med. Imaging* **39**(3), 668–677 (2020)
17. Ning, L., Westin, C.F., Rathi, Y.: Characterization of b-value dependent T2 relaxation rates for probing neurite microstructure. *bioRxiv*. Cold Spring Harbor Laboratory (2022)
18. Palombo, M., et al.: SANDI: a compartment-based model for non-invasive apparent soma and neurite imaging by diffusion MRI. *Neuroimage* **215**, 116835 (2020)
19. Pizzolato, M., Andersson, M., Canales-Rodríguez, E.J., Thiran, J.P., Dyrby, T.B.: Axonal T2 estimation using the spherical variance of the strongly diffusion-weighted MRI signal. *Magn. Reson. Imaging* **86**, 118–134 (2022)
20. Reymbaut, A.: Diffusion anisotropy and tensor-valued encoding. In: Topgaard, D. (ed.) *New Developments in NMR*, pp. 68–102. Royal Society of Chemistry, Cambridge (2020)
21. Slator, P.J., et al.: Combined diffusion-relaxometry microstructure imaging: Current status and future prospects. *Magn. Reson. Med.* **86**(6), 2987–3011 (2021)
22. Sotardi, S., et al.: Voxelwise and regional brain apparent diffusion coefficient changes on MRI from birth to 6 years of age. *Radiology* **298**(2), 415 (2021)
23. Tavakoli, M.B., Khorasani, A., Jalilian, M.: Improvement grading brain glioma using T2 relaxation times and susceptibility-weighted images in MRI. *Inform. Med. Unlocked* **37**, 101201 (2023)
24. Upadhyay, N., Waldman, A.: Conventional MRI evaluation of gliomas. *Br. J. Radiol.* **84**(2), S107–S111 (2011)
25. Veraart, J., Novikov, D.S., Fieremans, E.: TE dependent Diffusion Imaging (TEdDI) distinguishes between compartmental T2 relaxation times. *Neuroimage* **182**, 360–369 (2018)
26. Veraart, J., et al.: Noninvasive quantification of axon radii using diffusion MRI. *eLife* **9**, e49855 (2020)
27. Weisskoff, R., Zuo, C.S., Boxerman, J.L., Rosen, B.R.: Microscopic susceptibility variation and transverse relaxation: theory and experiment. *Magn. Reson. Med.* **31**(6), 601–610 (1994)
28. White, N.S., Leergaard, T.B., D'Arceuil, H., Bjaalie, J.G., Dale, A.M.: Probing tissue microstructure with restriction spectrum imaging: histological and theoretical validation. *Hum. Brain Mapp.* **34**(2), 327–346 (2013)
29. Zhang, H., Schneider, T., Wheeler-Kingshott, C.A., Alexander, D.C.: NODDI: practical in vivo neurite orientation dispersion and density imaging of the human brain. *Neuroimage* **61**(4), 1000–1016 (2012)